CHAPTER 8

TECHNIQUES IN ANALYZING THE NEOCORTICAL FINE-STRUCTURE

F. KRUGGEL
Interdisciplinary Center for Clinical Research, University of Leipzig,
Inselstrasse 22, D-04103 Leipzig, Germany
Tel: +49-341-9715992
frithjof.kruggel@medizin.uni-Leipzig.de

Cytoarchitectonic fields of the human neocortex are defined by characteristic variations in the composition of a general six-layered structure. It is commonly accepted that these fields correspond to functionally homogeneous entities. Diligent techniques were developed to characterize cytoarchitectonic fields by staining sections of *post-mortem* brains and subsequent statistical evaluation. Fields were found to show a considerable interindividual variability in extent and relation to macroscopic anatomical landmarks. Recent advances in high resolution magnetic resonance (MR) imaging techniques have demonstrated the feasibility to study the neocortical fine-structure in anatomical MR images, thus, defining cytoarchitectonic fields by *in vivo* techniques. The current status of this research is summarized in terms of image acquisition, image analysis, evaluation and validation.

Keywords: Magnetic resonance imaging; high-resolution anatomical imaging; neocortical fine-structure; myeloarchitecture of the human brain; Brodmann areas; image segmentation; statistical classification.

1. Introduction

When discussing structure-function relationships in the brain, it is important to distinguish between anatomical and functional variability. While the latter is related to inter-individual differences in the implementation of a cognitive task in the brain, task-solving strategies, motivation etc., the former term addresses inter-individual differences in the pattern, location and extent of functional activations. There is little doubt that there is a close correspondence between the functional organization of the neocortex and the cytoarchitectonic fields, which have been characterized by different histological staining techniques (e.g. Nissl staining) in *post-mortem* brains during the last 100 years.[5,27,34,35] Cytoarchitectonic fields are defined by varying compositions of the general six-layered fine-structure of the neocortex characterized by the properties and densities of neurons and their connecting fibers (see Fig. 1). One of the most recent techniques for delineating the borders of cytoarchitectonic fields is called objective cytometry.[28,29] This technique examines radial intensity profiles across the neocortical sheet in stained brain sections that are statistically

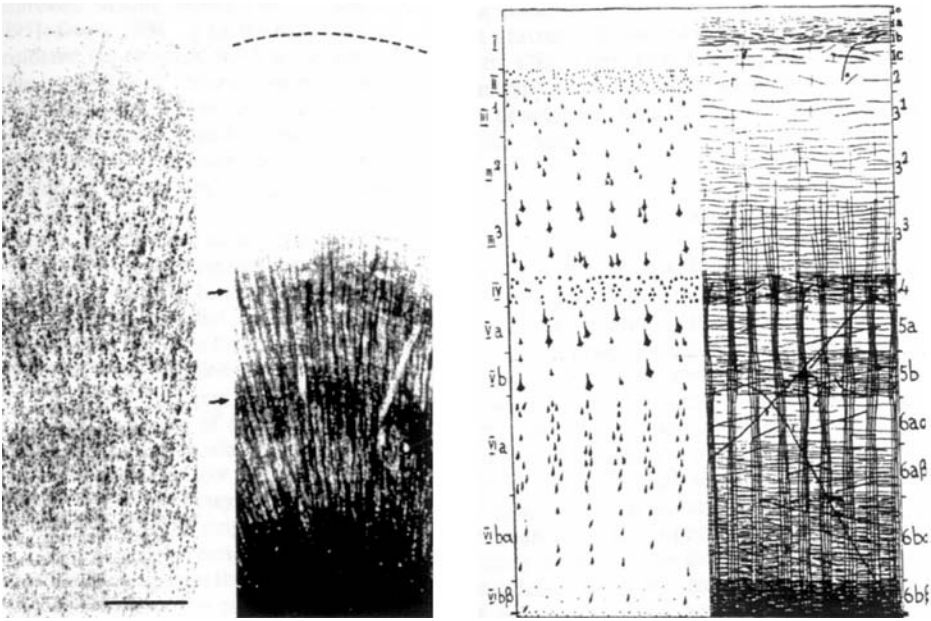

Fig. 1. Left: Nissl and myelin preparation from a section of Area 7 (reproduced from Hellwig, 1993). Right: Basic scheme of the cyto- and myeloarchitecture of an association cortex (reproduced from Vogt and Vogt, 1919). Note the similarity of myelin stained slices with MR images of a fixated brain (e.g. see Fig. 3).

compared along a trajectory on the surface. Local maxima in the classification function indicate a border between two fields.

It is now well accepted these fields show a considerable interindividual variability with respect to macroscopic landmarks such as sulcal and gyral borders and their substructures.[3,24–26,36] It is an open issue whether macroscopic landmarks are sufficient for describing the position of functional activation (e.g. as revealed by *in vivo* MR imaging), or whether it is necessary to resort to atlas-based descriptions of cytoarchitectonic fields that are obtained *in vitro* from *different* subjects in the form of a probabilistic map.

Myelin preparations of brain slices reveal the "wiring" of the neurons. Note that a myelin preparation and a Nissl staining (see Fig. 1) show complementary structural aspects. Neocortical subdivisions by cytoarchitecture resemble those based on myeloarchtecture.

Histological techniques offer a spatial resolution which is well beyond the limits of current (macroscopic) anatomical MR imaging protocols. However, recent investigations demonstrated that a spatial resolution of 0.25 mm (i.e. a matrix of 1024×1024 voxels) for anatomical scanning is feasible, and even 0.10 mm voxel dimensions may be aimed at for regional measurements. At this resolution, the neocortical sheet is mapped as a layer of 12 (or even, 30) voxels, which may be sufficient to recognize the layer structure of the cortex. Suitable image post-processing

techniques may be designed to classify cortical intensity profiles, and thus, to define borders of cytoarchitectonic fields *in vivo*.

The work described here investigates the feasibility of segmenting the neocortical fine-structure in MRI data. To achieve a high spatial resolution at a reasonable signal-to-noise ratio without restrictions in scanning time, we have resorted to examine a fixated brain hemisphere. Since the MR signal strength is related to the local cellular environment (e.g. biopolymer content) in a volume, it is not unreasonable to assume that stained histological intensity profiles and MRI intensity profiles show some similarity, albeit at a much lower spatial resolution. Thus, we will compare previously published results obtained by objective cytometry[1,2,11,38] with an MRI-based neocortical fine-structure analysis.

2. Materials and Methods

2.1. *Brain preparation and scanning*

An isolated left brain hemisphere (female, 72 years of age) obtained from a routine autopsy was fixated in formalin and embedded in a small container in agar gel, taking care of removing small air bubbles located in deep sulci by ultrasound immersion. MR acquisition was performed on a Bruker 3T Medspec 100 system equipped with a bird cage quadrature coil. Our standard T_1-weighted 3D MDEFT protocol[19] was used, except that the spatial resolution was increased (FOV $96 \times 192 \times 128$ mm, matrix $256 \times 512 \times 512$, voxel size $0.375 \times 0.375 \times 0.25$ mm) and the scanning time set to 12 h.

2.2. *Preprocessing*

The first steps consist of preprocessing the acquired image data: data format conversion, interpolation, and correction of intensity inhomogeneities. All processing steps were performed with our proprietary image processing system called BRIAN.[15] First, data were converted from the scanner into our proprietary data format, using an optimal histogram translation from 16 to 8 bit per pixel. Ten percent of the low-intensity voxels were mapped to 0, 1% of the high intensity voxels to 255, the interval in-between mapped linearly. Then, sagittal slices were transposed into the axial direction while interpolating voxels to an isotropical resolution of 0.25 mm using fourth-order b-spline interpolation,[32] and cropped to a minimum bounding box enclosing the hemisphere of $276 \times 608 \times 384$ voxels.

Inhomogeneities of the $B1$ scanner field lead to contrast differences within the measurement volume (see Fig. 2, top). For our dataset, the contrast ratio of white matter to grey matter varied up to 50%. To correct for these differences, a modified version of the "adaptive fuzzy c-means" algorithm[23] was employed. It clusters data by computing a measure of membership, called the *fuzzy membership*, at each voxel for a specified number of classes C. The fuzzy membership function u, constrained to be between zero and one, reflects the degree of similarity between a voxel intensity y_i and the prototypical data value m_c or *centroid*, of its class. In this simple form, the

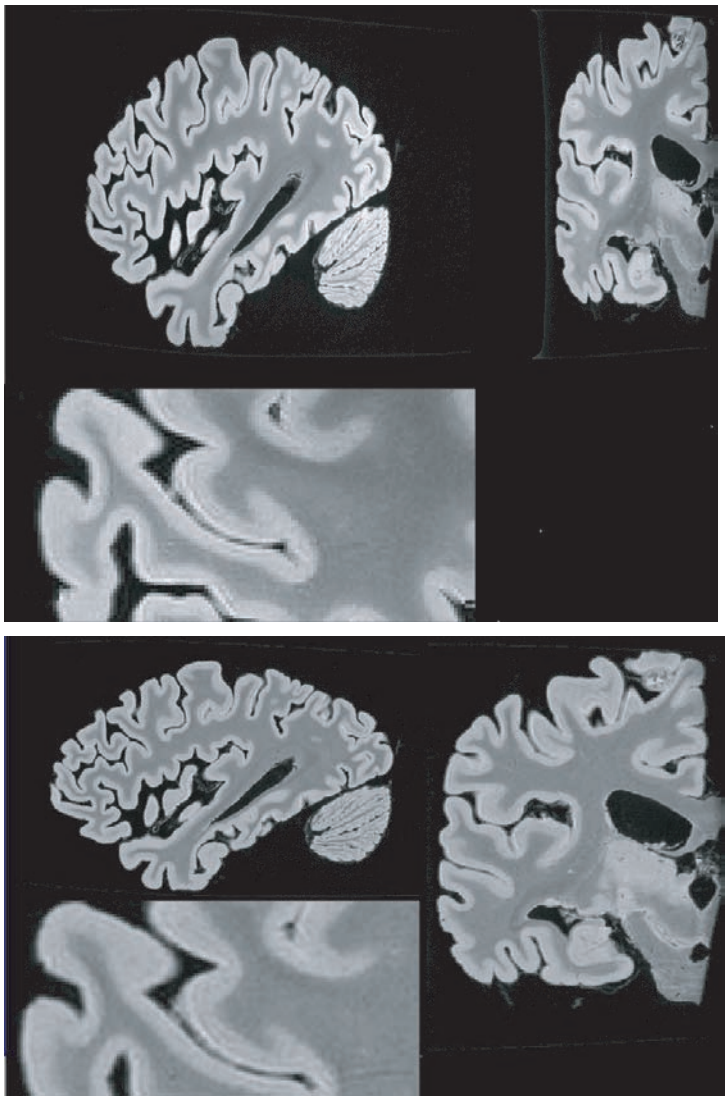

Fig. 2. Top: Sagittal, coronal and enlarged axial slice of the original high resolution MRI dataset. Note the anisotropy of the voxel size and the intensity inhomogeneities (esp. close to the midline and in cranio-caudal direction). Below: corresponding views of the interpolated and intensity-corrected dataset.

cost function P_{FCM} for this "fuzzy c-means" classification problem is:

$$P_{FCM} = \sum_{i \in \Omega} \sum_{c=1}^{C} u_{ic}^2 (y_i - m_c)^2, \tag{1}$$

where Ω denotes the image domain. Now, we assume that a class-independent but spatially variable gain field g modulated measured voxel intensities. We further

empose a smoothness constraint to this field in the form of a Tikhonov–Philips regularizer:

$$P_{AFCM} = \sum_{i\in\Omega}\sum_{c=1}^{C} u_{ic}^2 (y_i - g_i m_c)^2 + \lambda_1 \sum_{i\in\Omega}\sum_{r=1}^{3} (D_r \star g)_i^2 + \lambda_2 \sum_{i\in\Omega}\sum_{r=1}^{3}\sum_{s=1}^{3} (D_r \star D_s \star g)_i^2, \tag{2}$$

where D_r (D_s) is a known finite differencing operators along the rth (sth) dimension, and $\star$ is the convolution operator. Now, the estimation algorithm consists of the following steps:

(1) Provide initial values for the centroids $m_c, c = 1, \ldots, C$ and the gain field g_i.
(2) Compute membership functions:

$$u_{ic} = \frac{(y_i - g_i m_c)^{-2}}{\sum_{k=1}^{C} (y_i - g_i m_k)^{-2}}, \quad \forall\, i \in \Omega \text{ and } c = 1, \ldots, C. \tag{3}$$

(3) Compute new centroids:

$$m_c = \frac{\sum_{i\in\Omega} u_{ic}^2 g_i y_i}{\sum_{i\in\Omega} u_{ic}^2 g_i^2}, \quad \forall\, c = 1, \ldots, C. \tag{4}$$

(4) Compute a new gain field:

$$\sum_{c=1}^{C} u_{ic}^2 y_i m_c = g_i \sum_{c=1}^{C} u_{ic}^2 m_c^2 + \lambda_1 (H_1 \star g)_i + \lambda_2 (H_2 \star g)_i, \tag{5}$$

where the convolution kernels H_1 and H_2 are given by:

$$H_1^{1,3} = \begin{pmatrix} 0 & 0 & 0 \\ 0 & -1 & 0 \\ 0 & 0 & 0 \end{pmatrix}, \quad H_1^{2} = \begin{pmatrix} 0 & -1 & 0 \\ -1 & 6 & -1 \\ 0 & -1 & 0 \end{pmatrix},$$

$$H_2^{1,5} = \begin{pmatrix} 0 & 0 & 0 & 0 & 0 \\ 0 & 0 & 0 & 0 & 0 \\ 0 & 0 & 1 & 0 & 0 \\ 0 & 0 & 0 & 0 & 0 \\ 0 & 0 & 0 & 0 & 0 \end{pmatrix}, \quad H_2^{2,4} = \begin{pmatrix} 0 & 0 & 0 & 0 & 0 \\ 0 & 0 & 2 & 0 & 0 \\ 0 & 2 & -12 & 2 & 0 \\ 0 & 0 & 2 & 0 & 0 \\ 0 & 0 & 0 & 0 & 0 \end{pmatrix},$$

$$H_2^{3} = \begin{pmatrix} 0 & 0 & 1 & 0 & 0 \\ 0 & 2 & -12 & 2 & 0 \\ 1 & -12 & 42 & -12 & 1 \\ 0 & 2 & -12 & 2 & 0 \\ 0 & 0 & 1 & 0 & 0 \end{pmatrix}.$$

This system is solved using successive overrelaxation ($\omega = 1.75$). To speed up the solution, we used a 3-level multigrid solution scheme. Heuristically, we found $\lambda_1 = 20000, \lambda_2 = 200000$.

(5) If the algorithm has converged, then quit. Otherwise, goto step 2. Convergence is assumed if the biggest change in a class membership function is below 0.1. Typically, 20 iterations are required.

On output, we computed corrected intensities for the image $\hat{y}_i = y_i/g_i$ and obtained fuzzy membership functions for each voxel and class u_{ic}.

As with any variant of the c-means algorithm, a good initialization is required. We assumed that the average intensity within a subregion of the image is constant, i.e. is only affected by inhomogeneities. Thus, we computed the average foreground intensity for the whole image domain $\bar{y}_\Omega$ and within cubic subregions of 40^3 voxels ($\bar{y}_r$). The quotient $\bar{y}_r/\bar{y}_\Omega$ was used to initialize the gain field within this subregion. Based on this fixed setting for the gain g_i, an initial classification was computed by alternating steps 2 and 3 of the algorithm above.

The computation time for this 62 MB data volume was 2 h on a Linux system equipped with 2 GB RAM and a Athlon 1.5 GHz processor. Finally, we yielded a segmentation into three classes (class 1: background (BG), class 2: white matter (WM), class 3: grey matter (GM)) and an intensity-corrected version of the input image (see Fig. 2, below). Intensity inhomogeneities were less than 7% in this dataset.

2.3. *White matter segmentation*

The following steps aim at generating a raw segmentation of the hemisphere's white matter. We used the fuzzy membership function class 2 obtained from the segmentation procedure above. All voxels $u_{i2} \geq 0.5$ were selected as the initial WM segmentation. This dataset was scaled down by a factor of 2 to yield a spatial resolution of 0.5 mm. A morphological opening operator (radius 1 voxel) was used to remove small bridges. Connected components were labelled, and the biggest connected component was selected (see Fig. 3, top) as the raw WM segmentation.

The following steps are not required for the analysis of the neocortical fine-structure, but improve the quality of the GM and WM surfaces computed in the next processing steps.

To improve the visualization of the occipital and basal cortices, the brainstem and cerebellum were removed using an image editor.[15] Likewise, the inner ventricles and basal ganglia were filled. For standard *in vivo* MRI datasets, an automated procedure was developed to perform this task. However, fixating and embedding this hemisphere led to deformations, and thus, to violations of the anatomical heuristics incorporated in the automated algorithm that made hand-editing necessary here.

The resulting object should have a topological genus of 0 (i.e. have no holes or handles).[33] However, noise in the dataset and the thresholding operation on the fuzzy membership function introduce segmentation errors. In our case, the genus of the edited WM segmentation was 30. We removed these holes using a procedure similar to the one described by Shattuck and Leahy.[30] By changing 357 of 654000

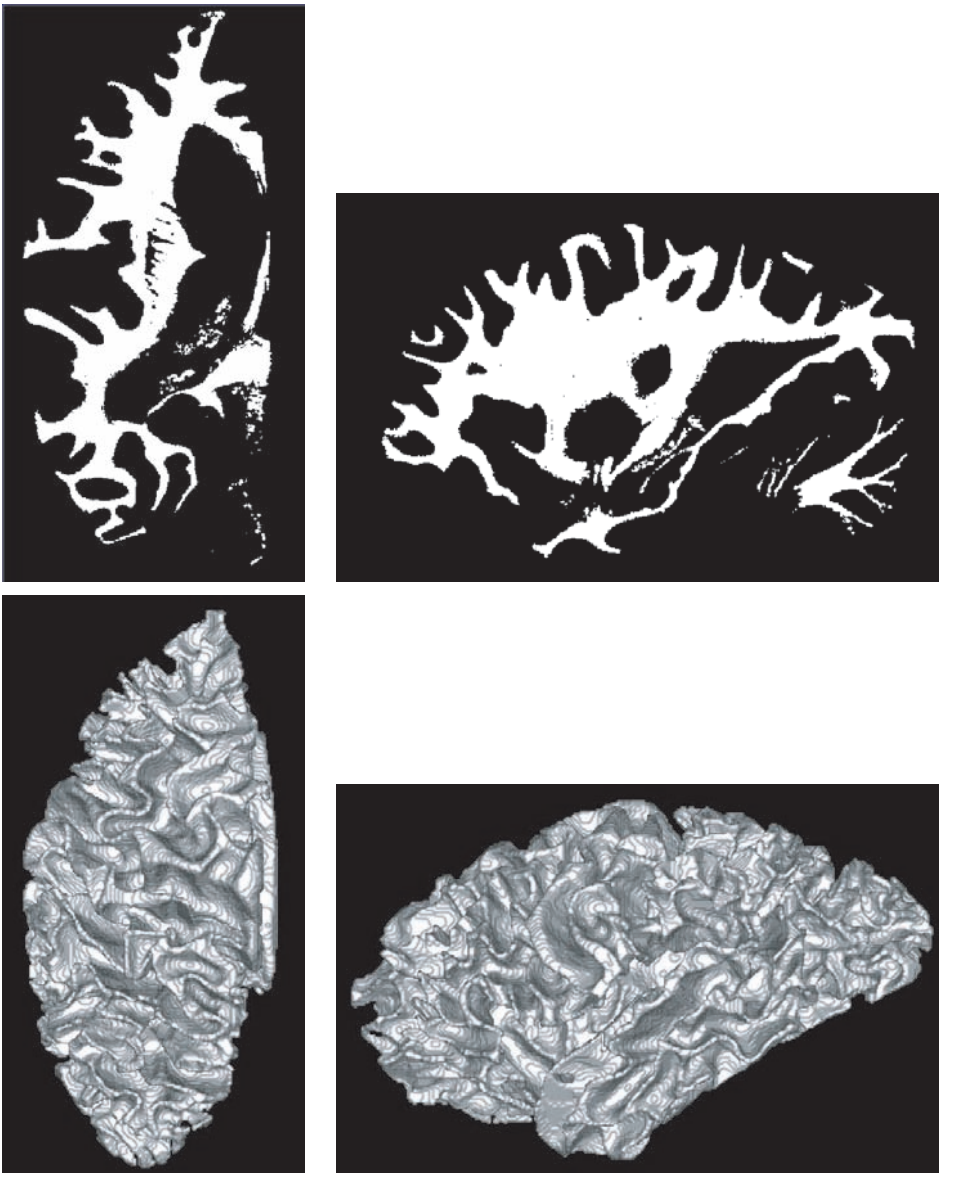

Fig. 3. Top: Axial (left) and sagittal (right) views of the raw white matter segmentation as a binary voxel volume. Below: Corresponding views of the initial WM/GM interface (721000 triangles). Note the "staircase" artifacts on the surface, a consequence of generating a surface from a binary voxel volume.

voxels, we obtained a $C18$-connected object[33] of genus 0, corresponding to a white matter segmentation in binary voxel space.

2.4. *Segmentation of basins*

Sulci and gyri allow introducing a macroscopic subdivision of the neocortical surface. In order to study the issue how much microstructurally defined fields respect macroscopic borders, we computed a segmentation of the white matter surfaces into basins. Basins are substructures of sulci, i.e. one or more basins line up as a classical sulcus.[20] Basins are relatively simple to construct from a white matter segmentation. In a nutshell, the sulcal compartment is determined by morphological closing of the WM segmentation using a spherical kernel of 14 mm diameter. In this compartment, a constrained distance transform is computed subject to the white matter segmentation. Local maxima of this constrained distance transform correspond to the deepest points in the sulci, and each of these maxima marks a basin. Starting from these points, a classical concurrent region growing algorithm fills these basins. Typically, 100–150 basins are found per hemisphere. Four neuroanatomically relevant regions were selected as examples and compiled in Fig. 4, the central sulcus, the calcarine fissure, and the pars triangularis and opercularis of the inferior frontal gyrus.

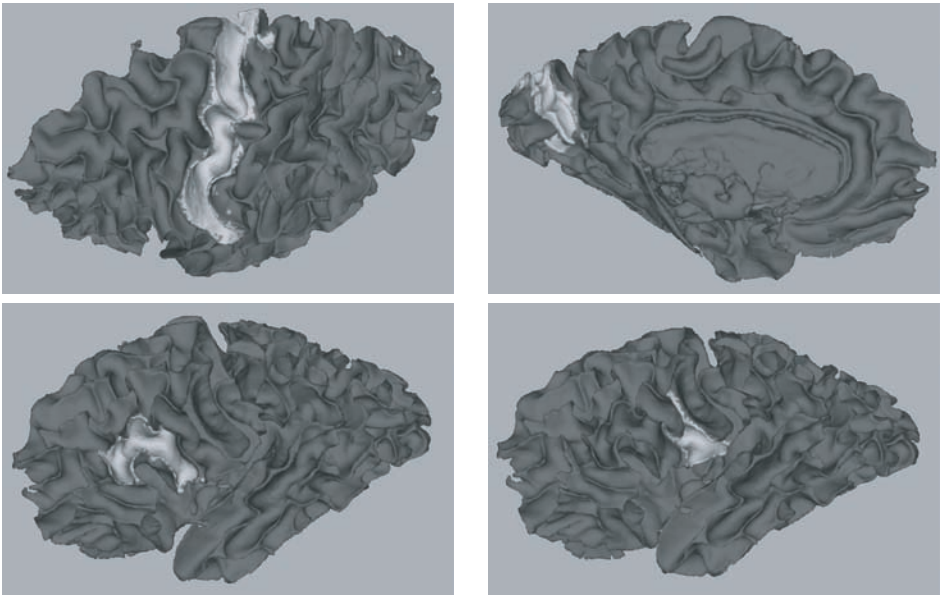

Fig. 4. Basin segmentation of the central sulcus (top left), calcarine fissure (top right), inferior frontal gyrus, pars triangularis (bottom left), inferior frontal gyrus, pars opercularis (bottom right). For visualization, detected basins were mapped on the white matter surface (compare with Fig. 5, top).

2.5. *Computation of the interfaces*

The following steps aim at generating the interfaces between white/grey matter (WM/GM) and grey matter/background (GM/BG) as polygon meshes in 3D. The rationale for generating these interfaces is to define starting points and directions of intensity profiles that run radially through the cortex.

A triangulated surface was generated from the binary white matter segmentation using the "Marching Cubes" algorithm.[21] Because the original algorithm may introduce ambiguities in the triangulation, a variant that preserves the original topology was employed here.[6] We yielded an initial surface close to the WM/GM interface consisting of 721000 triangles.

An improved model of the WM/GM interface was obtained by treating this initial mesh as a deformable model.[31] With modifications, we follow the ideas of Xu *et al.*[37] and Dale and Sereno[7] here. On any vertex v_0 in the mesh, internal and external forces act until a balance is acheived. The internal force F_{int} tries to center a vertex among its edge-connected neighbors $v_i, i = 1, \ldots, N$:

$$F_{int} = \frac{1}{N} \sum_{i=1}^{N} (v_i - v_0). \tag{6}$$

The first external force $F_{ext,1}$ tears a vertex outwards in the direction of its surface normal n_0. This force is exerted by an intensity-gradient field f, which is computed from a convolution of the intensity-corrected image I with a Gaussian kernel G: $f = \nabla(G \star I)$:[37]

$$|F_{ext,1}| = \langle f(v_0), n_0 \rangle, \tag{7}$$

where $\langle , \rangle$ denotes the scalar product. The second external force $F_{ext,2}$ captures the surface within a narrow range around an image intensity I_{lim}:

$$|F_{ext,2}| = \tanh(\kappa(I(v_0) - I_{lim})), \tag{8}$$

where κ corresponds to the capturing range and is related to the noise level in the data set. $F_{ext,2}$ pushes a vertex in the direction of the surface normal until a position with intensity I_{lim} is reached. A suitable value for I_{lim} was chosen as the average of the class center intensities for WM and GM in the initial segmentation step. Forces are weighted to ensure good convergence properties during iterations t of the surface adaption process:

$$v_0^{(t+1)} = v_0^{(t)} + w_1 F_{int} + n_0(w_2 |F_{ext,1}||F_{ext,2}| - w_3 |F_{ext,2}|). \tag{9}$$

The image gradient force $|F_{ext,1}|$ is weighted by the intensity force $|F_{ext,2}|$ in order to reduce the outward-driving force adaptively when the destination intensity range is reached. This constraint also reduces the chance of introducing self-intersections.

For generating the WM/GM interface, we used parameters: $w_1 = 0.1$, $w_2 = 0.0001$, $w_3 = 0.02$, $I_{lim} = 130$, $\kappa = 10$, and 200 iterations for convergence. Starting again from the initial mesh, we obtained the GM/BG interface using $I_{lim} = 195$, and 1000 iterations for convergence.

Finally, we reduced the high resolution of these interfaces to 200000 triangles each, i.e. one triangle corresponds to a surface area of about 1 mm^2. We used a variant of the edge contraction method described by Garland and Heckbert.[10] This algorithm respects the local curvature by using a quadrics-based error metric. Their approach was enhanced by an additional criterion that ensures topology preservation during mesh simplification. Example views of both interfaces are shown in Fig. 5.

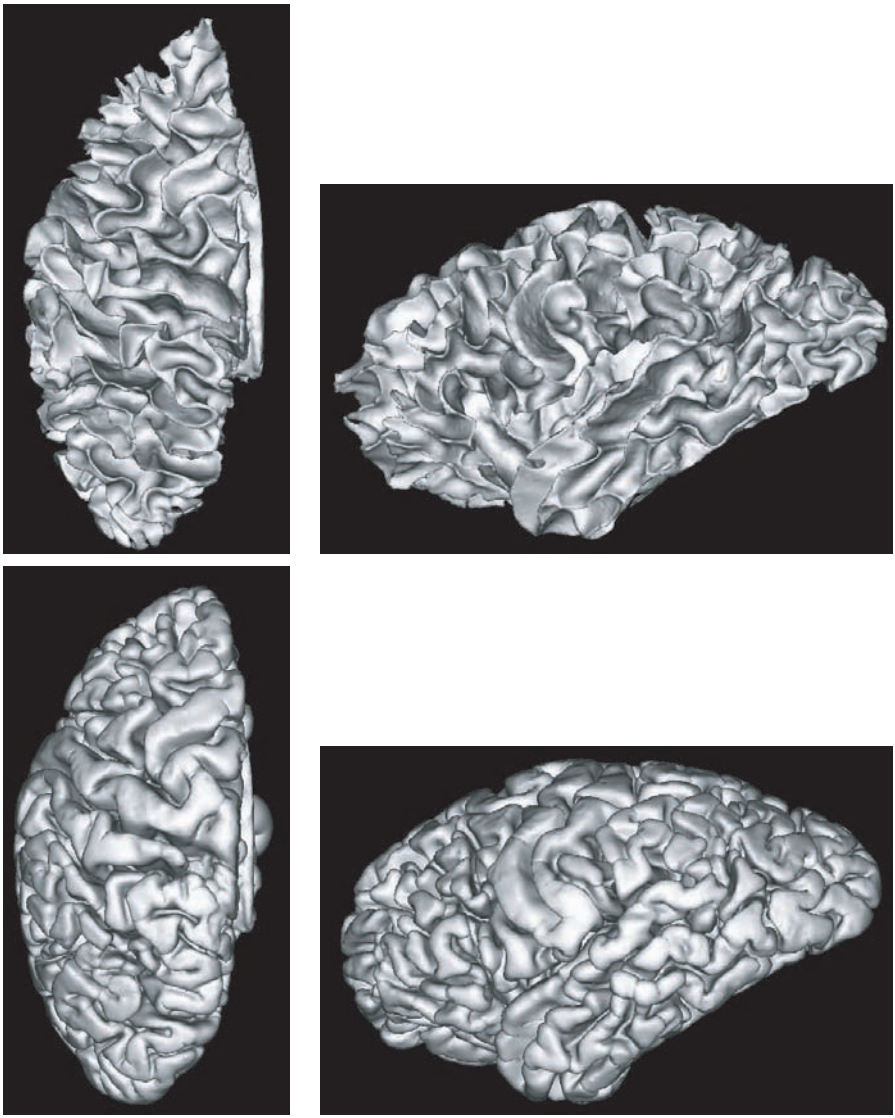

Fig. 5. Top: Axial (left) and sagittal (right) views of the adapted WM/GM interface (200000 triangles). Below: Corresponding views of the adapted GM/BG interface. In comparison with Fig. 3, surfaces now appear smooth, due to refinement as a deformable model.

2.6. *Determination of the neo-cortical intensity profiles*

The space between the interfaces WM/GM and GM/BG is occupied by the neocortex. To describe the local properties of the fine-structure, we computed intensity profiles that run radially through the cortex. These profiles were characterized by a sparse set of parameters, and classified locally into surface patches that were compared with the known extent of neurofunctional areas.

Starting from each vertex on the interface WM/GM, we walk 3 mm outwards in the direction of the vertex normal, and construct a sphere of 5 mm around this point. All triangles of the interface GM/BG that intersect with this sphere are collected in a list. Then, the shortest distance between the vertex on the interface WM/GM and each triangle is determined.[8,16] The shortest path of all triangles in the list defines the direction of the profile. Along this direction, we sampled intensity values from the intensity-corrected dataset obtained in the segmentation step (see Sec. 2.2). In order to correct segmentation errors introduced in the steps above, we re-determined the local transition between WM and GM resp. GM and BG. Thus, sampling started 2 mm before the position of the vertex on interface WM/GM (i.e. in the white matter), and ended 8 mm after this position (i.e. within the background). Points were sampled at regular intervals of 0.025 mm using trilinear interpolation. A typical profile through the visual cortex is shown in Fig. 6.

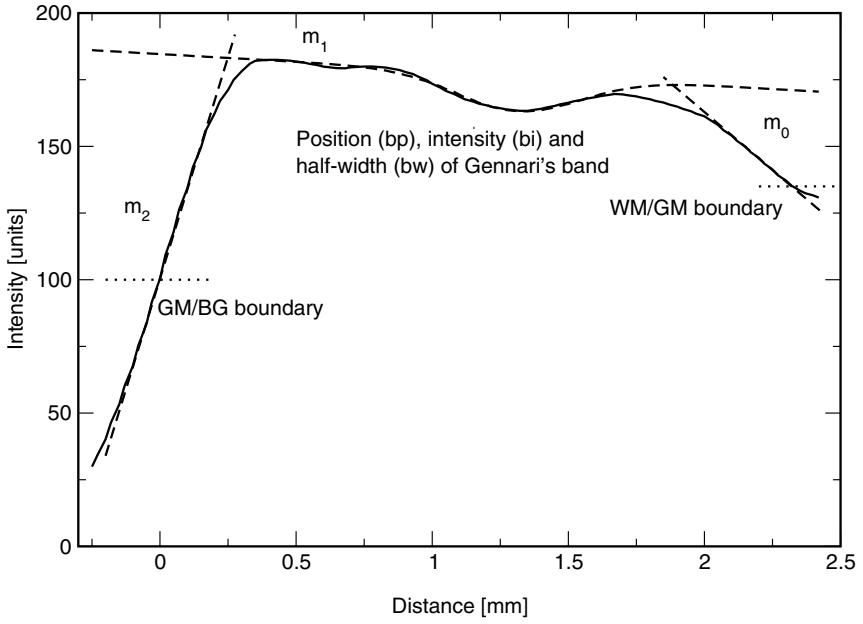

Fig. 6. Example intensity profile across Area 17. The rising flank (on the right) crosses the WM/GM border, while the slope of the intra-cortical segment is comparatively flat. The falling flank mostly results from the partial volume effect on the GM/BG boundary. A Gaussian function is used to model the position, intensity and width of intra-cortical bands, such as Gennari's band.

Starting from the low-intensity white matter, the rising flank (on the right) crosses the WM/GM border, while the slope of the high-intensity intra-cortical segment is comparatively flat. The falling flank mostly results from the partial volume effect on the GM/BG boundary. In order to define the WM/GM and GM/BG boundary points consistently, lines were adaptated to the rising flank of the profile (at the WM/GM boundary) and to the falling flank (corresponding to the GM/BG boundary, see Fig. 6). The exact position of the WM/GM boundary was computed at intensity $I = 135$, for the GM/BG-boundary at intensity $I = 100$, and their distance was recorded as the local cortical thickness th. Because layers occupy a rather constant *relative* portion of the cortex,[29] the profile was resampled at 1% intervals of th between both boundaries. In summary, we obtained for each vertex on the WM/GM interface the cortical thickness and a spatially normalized intensity profile of 101 data points.

When analyzing this one-dimensional signal, a number of special cases and exceptions had to be taken into account:

- There is no neocortex at this position (i.e. at the cut through the corpus callosum in the midline, at the brainstem). This case is easily detected, because the intermediate high-intensity segment is missing or very short (<0.5 mm).
- Two banks of a sulcus touch (i.e. there is no BG adjacent to GM). Here, we extrapolated the GM/BG-boundary point at $I = 100$, based on the slope of the falling flank.
- Artifacts may disturbe a profile (i.e. a cut or a tear through the cortex, an air bubble trapped in a sulcus). In these cases, an "unusual" formation of a profile is detected.

For any of these exceptions, we suppressed the resulting profile at this position.

Finally, intensity profiles were characterized for statistical evaluation by a sparse set of parameters:

- the cortical thickness th;
- the slope of the rising flank at the WM/GM boundary m_0 (see Fig. 6);
- the slope of the intra-cortical portion m_1;
- the slope of the falling flank at the GM/BG boundary m_2; and
- the position (bp), intensity (bi) and width (bw) of an intra-cortical band were determined by adaptation of a Gaussian function to the intra-cortical profile segment:

$$I = m_1 * x + n_1 - bi * \exp\left(-\frac{(x - bp)^2}{bw^2}\right). \tag{10}$$

Powell's algorithm was used to find optimized parameters.

2.7. *Classification of the neo-cortical fine-structure*

The final step consisted of a regional subdivision of profiles. We hypothesized that profiles within a cortical field exhibit a relatively high similarity.

Cortical areas with similar fine structure were determined by comparing local profile properties with those of a template region. To characterize the template, profile properties were collected from a surface patch of 5 mm radius around a manually specified position (typically, 60–100 vertices). This template region was selected at a position where a specific functional area is expected with high probability, based on prior neuroanatomical knowledge (i.e. for the motor cortex, a position at Broca's knee was selected). Properties of a local sample were collected from a given vertex and its first and second-order neighbors (typically, 10–30 vertices).

From a series of heuristical experiments, six statistical tests were selected to measure the similarity of the local region with the template:

- Pearson's correlation coefficient of the averaged profiles in both regions (z_1).
- Pearson's correlation coefficient of the first derivative of the averaged profiles (z_2).
- a t-test comparing the cortical thickness th of profiles in both areas (z_3).
- a t-test comparing the rising slope m_0 of profiles in both areas (z_4).
- a t-test comparing the intra-cortical slope m_1 of profiles in both areas (z_5) and
- a t-test comparing the band intensity bi of profiles in both areas (z_6).

A similarity measure was derived from the individual tests as:

$$z_{sim} = z_1 + z_2 - |z_3| - |z_4| - |z_5| - |z_6|. \tag{11}$$

If both regions contain similar profiles, z_3 to z_6 contribute values close to 0, while z_1 and z_2 provide positive scores, summing up to some (small) positive quantity. For dissimilar regions, negative similarity measures are expected. For performance reasons, we restricted the computation to the target region and its adjacent basins. A heuristically determined threshold was applied to z_{sim} to optimally discriminate between the target region and its neighbors.

3. Experiments

First, we performed a simple simulation experiment to verify the properties of the segmentation and classification algorithms. Then, we demonstrated the similarity of T_1-weighted MR images with myelin-stained brain slices. Finally, we selected three different anatomical regions that are well studied by histological techniques. We were interested in comparing intensity profiles with known descriptions of the local layer structure, and in comparing the extent of statistically homogeneous regions with known cytoarchitectonic fields.

3.1. *Evaluation*

In order to better understand the influence of the parameter settings on the resulting segmentation, we run a simple simulation study. A test object consisting of two folds was constructed (see Fig. 7).

The body of this object was set to an intensity similar to white matter ($I = 120$). A profile was added to the left fold with properties similar to those found in Area 17 (thickness 1.8 mm, intracortical intensity linearly increasing from $I = 135$ to $I = 200$, from 0.75 mm – 1.05 mm reduced by 30 intensity units to simulate Gennari's band). To the right fold, a profile resembling Area 18 was added (thickness 2.0 mm, intracortical intensity linearly increasing from $I = 135$ to $I = 200$). A multiplicative inhomogeneity field with parabolic cross-section was applied in z direction (i.e. along the fold) that led to an intensity decrease of 15% from the center to the upper and lower image border, similar to the inhomogeneity of 50% over 70 mm as in the original dataset (see Fig. 7, right). Finally, Gaussian distributed noise $\mathcal{N}(0, 5.5)$ was added.

This simulated dataset was analyzed with the same process chain as described above, using the same parameter settings. A position on the crown of the left fold (Area 17) was used as a template region. The distribution of z_{sim} for Area 17 and 18 is shown in Fig. 8.

Results were obtained for Area 17: $z_{sim} = 4.53 \pm 2.34$, for Area 18: $z_{sim} = -6.24 \pm 2.66$. A t-test of z_{sim} demonstrated highly significant differences between both areas ($p < 2.2\text{e-}16$, DOF = 3618). Figure 9 shows a segmentation of Area 17 using a threshold of $z > 0$. Note that z scores are independent of the z coordinate (the direction of the simulated intensity inhomogeneities).

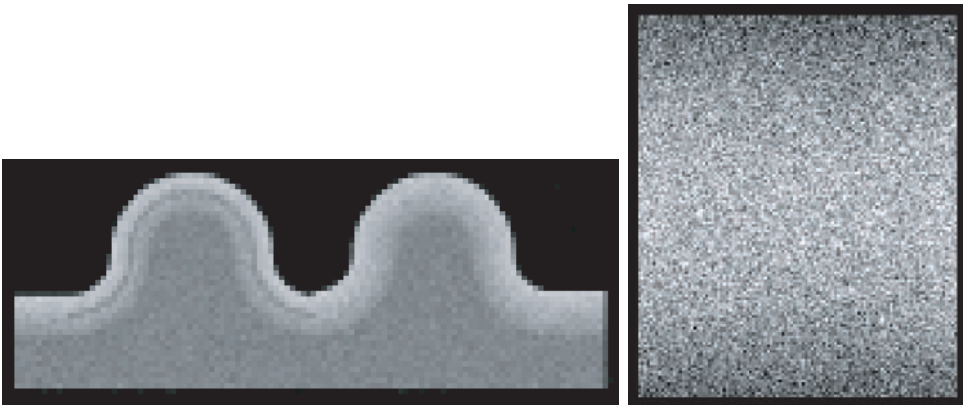

Fig. 7. Left: Cross-section through the test object in x-y plane. The left fold carries a simulated profile similar to Area 18, the right similar to Area 18. Right: Cross-section through the test object in x-z plane. Simulated inhomogeneities are visible as an intensity decrease from the center to the upper and lower image border.

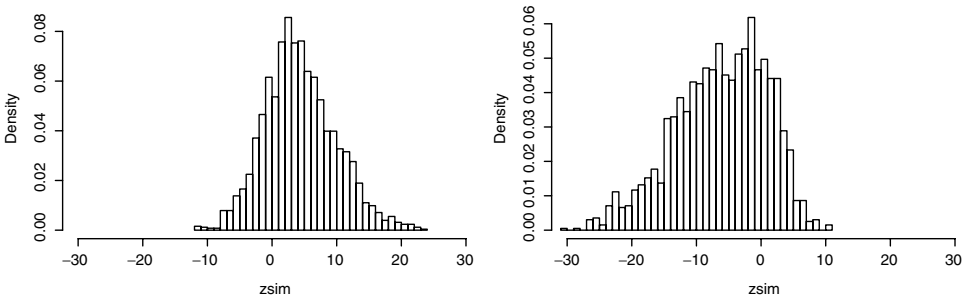

Fig. 8. Histogram of classification results z_{sim} for Area 17 (left) and Area 18 (right).

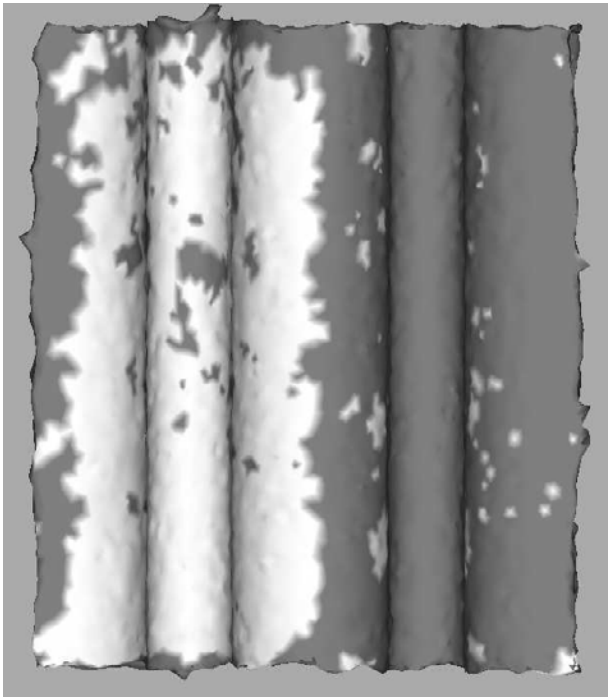

Fig. 9. Detected Area 17 (threshold $z_{sim} > 0$).

3.2. *Comparison of MR images and myelin-stained slices*

We validated some of our results by comparison of MRI data with stained brain slices. After MRI scanning, slices were cut from the fixated brain every 1.5 cm. Slices were embedded, myelin-stained, digitized using a PC scanner, and registered with the MRI volume. Here, a 2D–3D registration is necessary. We applied a low-dimensional transformation consisting of scaling, translation, and rotation. In addition, a deformation perpendicular to the slice plane on the basis of nine control

points was allowed. A cost function based on cross-correlation of both images was used, and a genetic algorithm was employed to optimize transformation parameters.

Example results from a coronal section through the occipital lobe are shown in Fig. 10. Note the striking qualitative similarity between the MR signal intensity and the contrast induced by staining. The correlation coefficient of both marked intensity profiles is 0.92. Note that the T_1 contrast is "inverted" by fixation: regions of higher neuron content (i.e. cortical layers 1–3, 5 and 6, basal ganglia) show a higher signal intensity than fiber-containing regions (i.e. the white matter).

3.3. *Visual cortex (Area 17)*

The visual cortex is distinguishable from the surrounding Area 18 by the presence of Gennari's band, which corresponds to layer IVb of this cortex and consists of

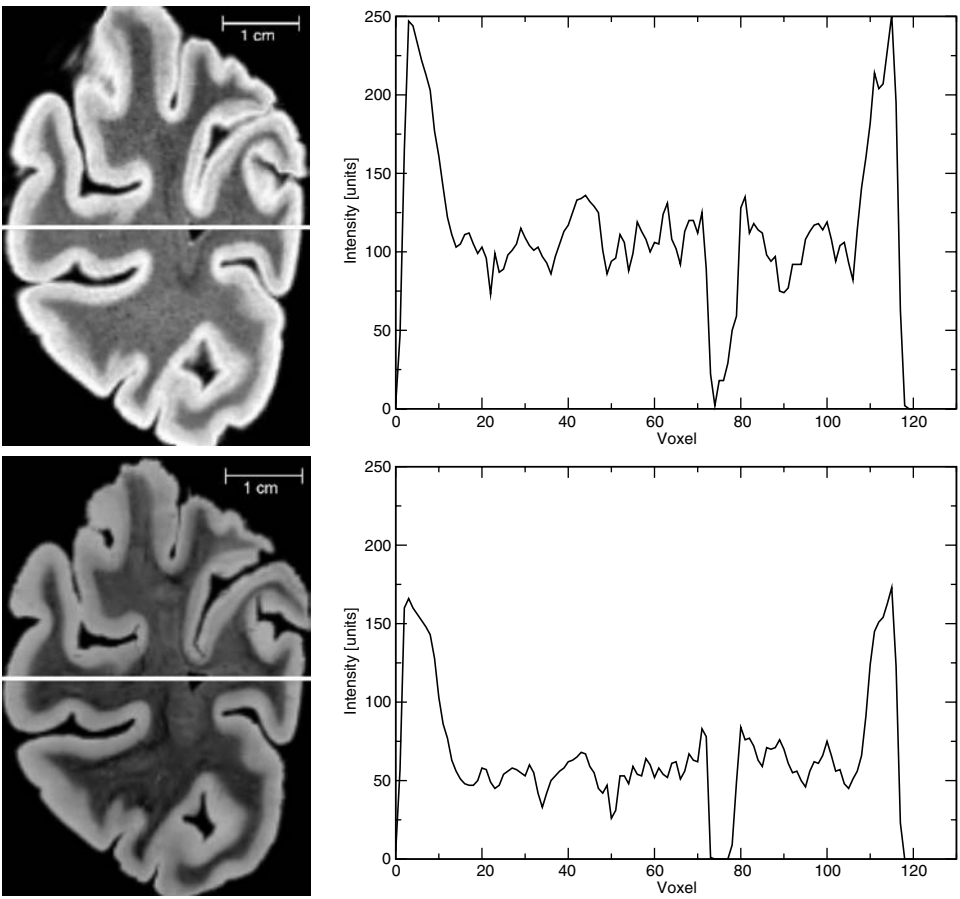

Fig. 10. Coronal section through the occipital lobe. MRI slice (top) and registered myelin-stained brain slice (below). Sample intensity profiles along the straight lines in both slices are shown on the right. The correlation coefficient of both profiles is 0.92. Note also the detection of Gennari's band in both modalities (in the banks of the calcarine fissure, upper right quadrant).

an intracortical horizontal fiber system. This structure is easily detected in the acquired MRI dataset as a darker band in the bright cortex (see Fig. 11).

By application of the procedures described above, the cortical thickness on the banks of the calcarine fissure was determined as 1.86 ± 0.10 mm (von Economo[35]: 1.84 mm), the position of the center of Gennari's band as $52 \pm 6\%$ (Zilles *et al.*[38]: 55%), and the thickness of this band as 0.30 ± 0.10 mm (Zilles *et al.*[38]: 0.28 mm).

The extent of Area 17 is described by von Economo[35] as located on the walls and lips of the calcarine fissure, and at the gyral crowns at the occipital pole. This description compares nicely with the automatically generated statistical classification as shown in Fig. 12.

3.4. *Motor and sensory cortex (Area 4 and 3)*

As a second example, we tried to differentiate the primary motor cortex (Area 4) on the anterior bank of the central sulcus from the somatosensory cortex (Area 3) on its posterior bank (see Fig. 13).

The most distinctive feature here is the cortical thickness: on the anterior bank, the motor cortex reaches values up to 3.8 mm, while the sensory cortex is less than 2.2 mm thick.[22,35] Intensity profiles in Area 4 mostly showed three maxima (see Fig. 13), which roughly correspond to the transition between layer II/III, layer III/V and layer V/VI as described by Amunts *et al.*[1] The somatosensory cortex on the posterior bank exhibited much less substructure.

A statistical classification was initialized by a manually specified region close to the hand field and yielded the full extent of the motor cortex well in agreement with previously published histological classifications (see Fig. 14). The border between the anterior and the posterior bank is sharp, although some small spots (esp. at crowns of other gyri) respond to this classificator as well.

3.5. *Broca's area (Area 44 and 45)*

As a final example, we selected Broca's speech region, which corresponds to Area 44 (the pars opercularis of the inferior frontal gyrus) and Area 45 (the pars triangularis of the inferior frontal gyrus).

As described by von Economo[35] and Amunts *et al.*,[3] the cortex of Area 44 is not sharply delineable from the white matter, which corresponds to a flat slope m_0 (see Fig. 15, bottom right). The cortex of Area 45 (see Fig. 15, bottom left) is thinner and features a more distinct horizontal layering.

For the delineation the extent of both areas, training regions were selected at characteristic positions as indicated in Fig. 15. Classification results are shown superimposed on the white matter surface in Fig. 16, separated for Area 45 (top) and Area 44 (below). Note that the detection of Area 45 is less specific and extends to adjacent sulci as well. However, detected Areas 45 and 44 are complementary in their extent, indicating that both are based on different properties of the fine-structure.

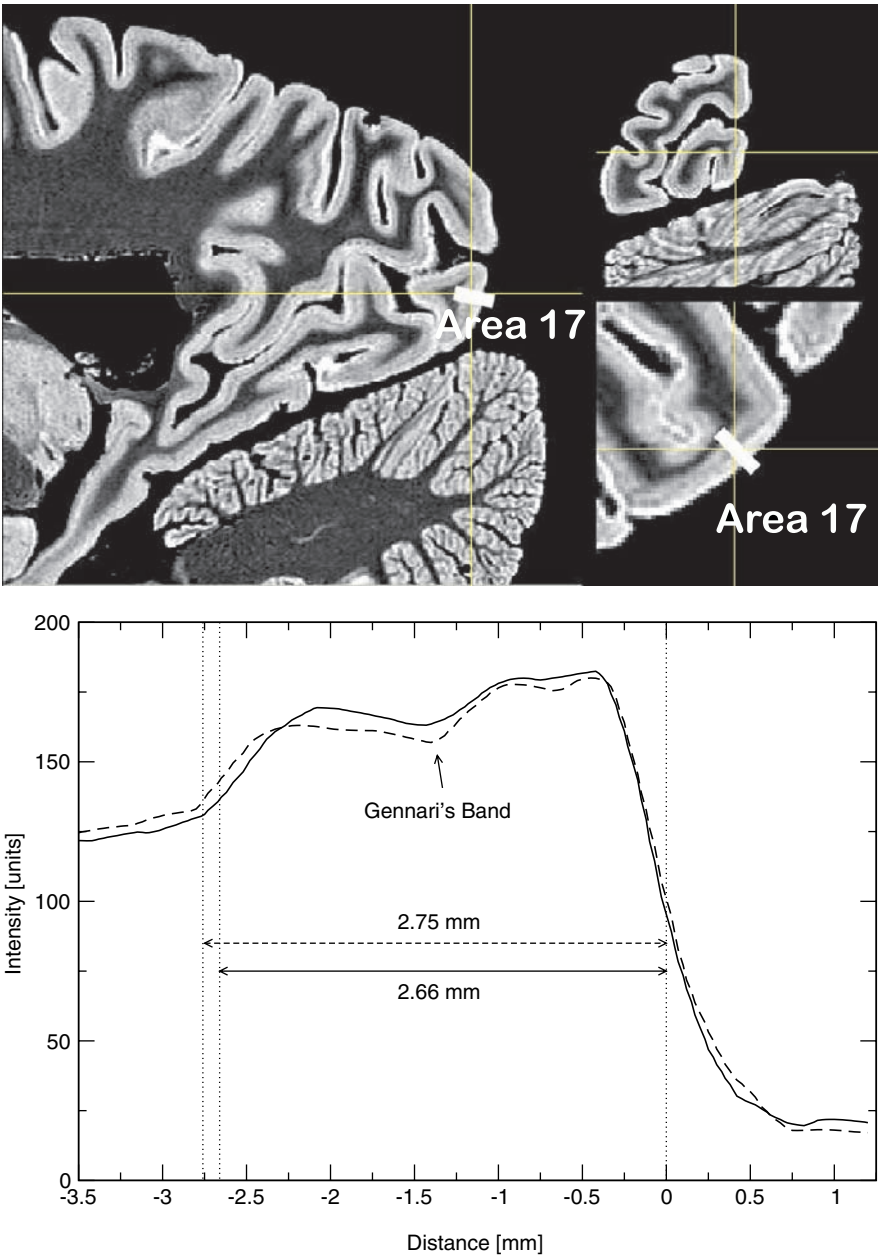

Fig. 11. Top: Sagittal, coronal and axial slice (enlarged) through the visual cortex. The position of the intensity profiles through Area 17 is marked by a white bar. Below: Two intensity profiles through Area 17. Gennari's band — visible as a dark horizontal line in the cortex — is indicated by an intensity drop at ≈52% of the cortical width.

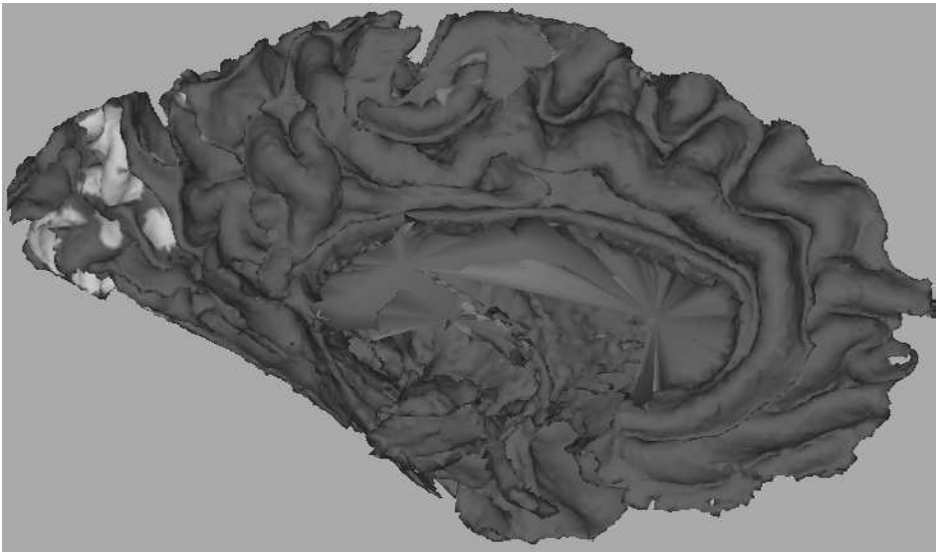

Fig. 12. Medial view of the white matter surface. The model region marked in Fig. 11 was used to detect Area 17 which is mapped in light grey at a detection threshold of $z_{sim} \geq -4$.

4. Discussion

Three results of this work are stated for discussion:

- "It is possible to reveal the neocortical fine-structure by high-resolution MR imaging."
  We have shown three examples of cortical regions where it is relatively easy to visually discriminate properties of the layer structure — even at a moderate spatial resolution of $0.375 \times 0.375 \times 0.25$ mm. Since our initial report,[17,18] this result was confirmed by three independent groups: using MR microscopy[9] *in vitro* at 9.4 T field strength and a spatial resolution of $0.078 \times 0.078 \times 0.500$ mm, using a standard T_1 weighted imaging protocol[4] (SPGR) *in vivo* at 3.0 T field strength and a spatial resolution of $0.350 \times 0.350 \times 0.600$ mm, and by comparing *in vivo* data (field strength 1.5 T, resolution $0.556 \times 0.556 \times 0.700$ mm) with *post-mortem* histological data.[36]
  The spatial resolution of the MRI data acquired here is $\approx$0.3 mm, and thus at least one order of magnitude lower than the resolution offered by histological techniques. However, these optical profiles are typically subsampled in space[28,29] in order to characterize gross features of layers. Results presented here suggest that most likely a microscopic resolution is not required if a classification of cortical areas is sought for. However, at a higher resolution (say, 0.1 mm), even more detail is revealed (see profiles in Ref. 9), leading to more powerful statistical classificators. It is ambitious but not impossible to implement scanning protocols

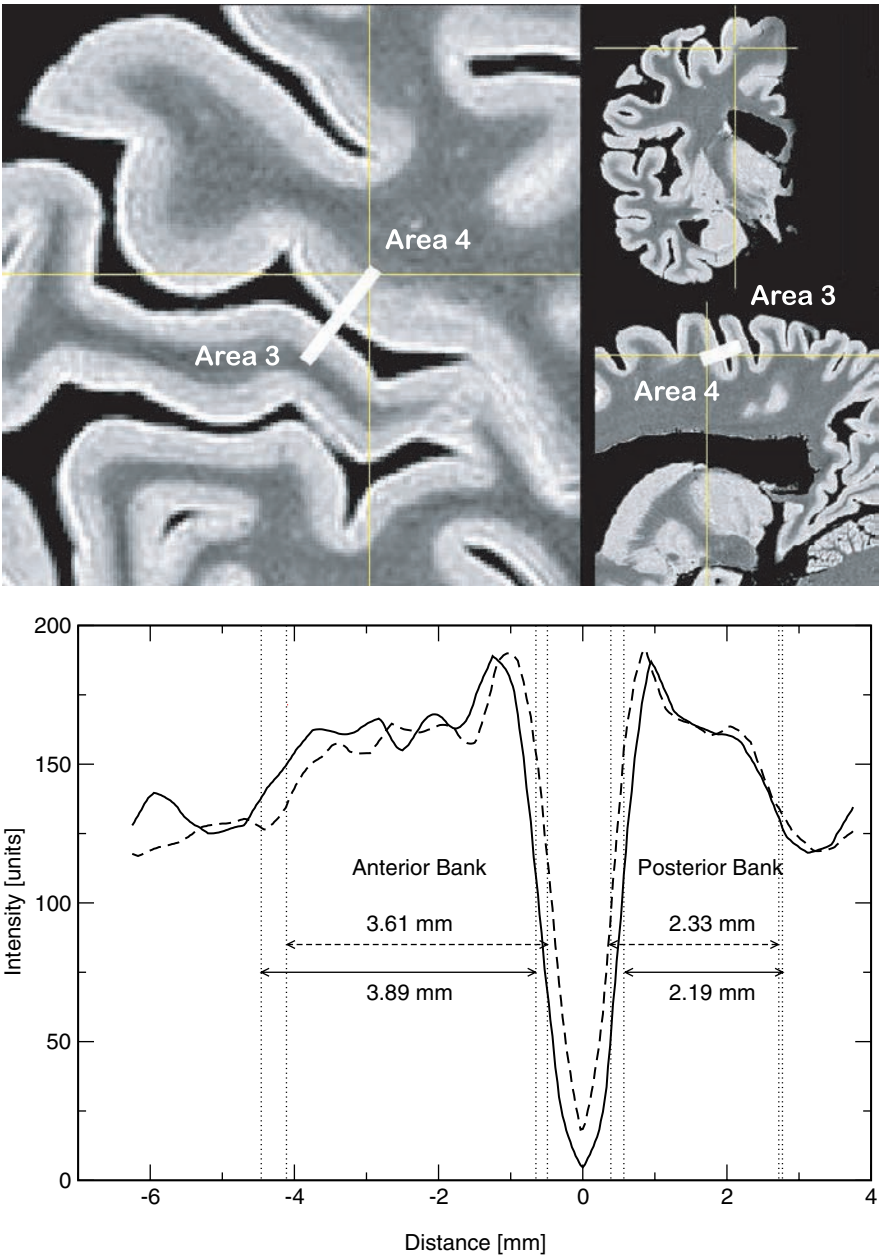

Fig. 13. Top: Sagittal, coronal and axial slice (enlarged) through the anterior (Area 4, motor cortex) and posterior (Area 3, sensory cortex) bank of the central sulcus. The position of the intensity profiles through Areas 4 and 3 is marked by a white bar. Below: Two intensity profiles through Area 4 and 3. The motor cortex is thicker than the sensory cortex and shows more substructure.

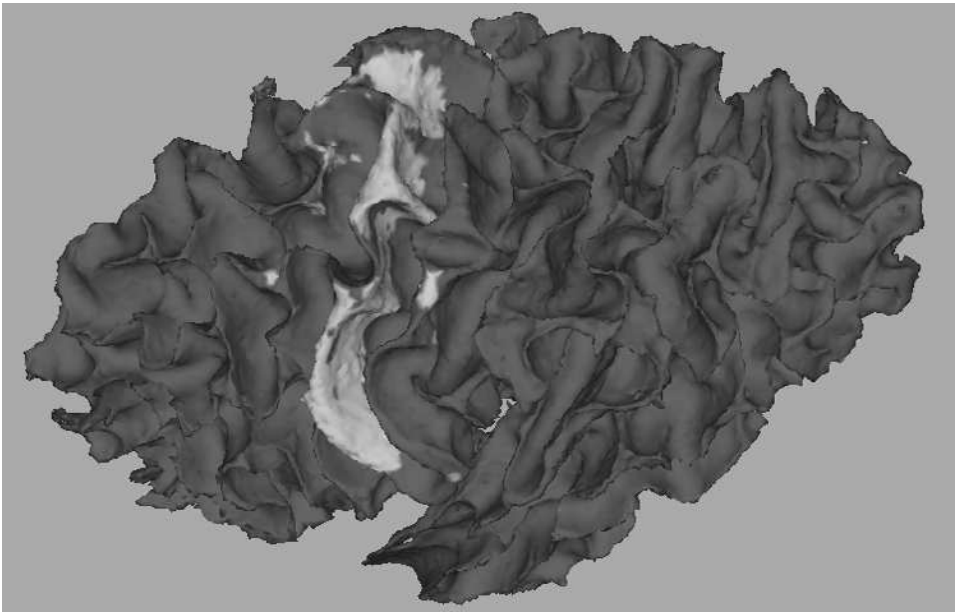

Fig. 14. Top lateral view of the white matter surface. Area 4 (detected from a model region at Broca's knee, see Fig. 13) is shown in light grey at a detection threshold of $z_{sim} \geq -4$.

for *in vivo* examination with a spatial resolution of 0.1 mm, at least if one focuses on a brain subregion (i.e. a lobe).

A critical issue of this study is to achieve a good signal-to-noise ratio (SNR) for acquiring high-resolution datasets of an acceptable quality. As for a given MR system, the MR signal strength is approximately proportional to the voxel volume, we simply scaled our standard scanning time of 20 min (1.5 mm^3 voxel volume) to 12 h (0.035 mm^3 voxel volume). However, the SNR measured here was about two times better compared with our standard MRI datasets, which is probably due to the small substance load in the coil, and the fact that an isolated brain was scanned. One may consider to reduce the scanning time to 3 h, accepting a SNR similar to those of standard MR datasets. We have rather chosen to conduct subsequent experiments with an isotropical resolution of 0.25 mm.

- "Intensity characteristics of T_1-weighted MR tomograms of formalin-fixated brains resemble those of myelin-stained brain slices that reveal the myeloarchitecture of the brain."

  We demonstrated an example of a myelin-stained brain slice that was digitized using a conventional PC scanner and then registered to the MRI volume data of the same brain. A striking qualitative similarity between the MR signal intensity and the contrast induced by staining was found. The correlation coefficient of the example intensity profile is 0.92. These findings were confirmed by Fatterpekar *et al.*[9] using MR microscopy and noted by Walters *et al.*[36]: "Equivalent intensity

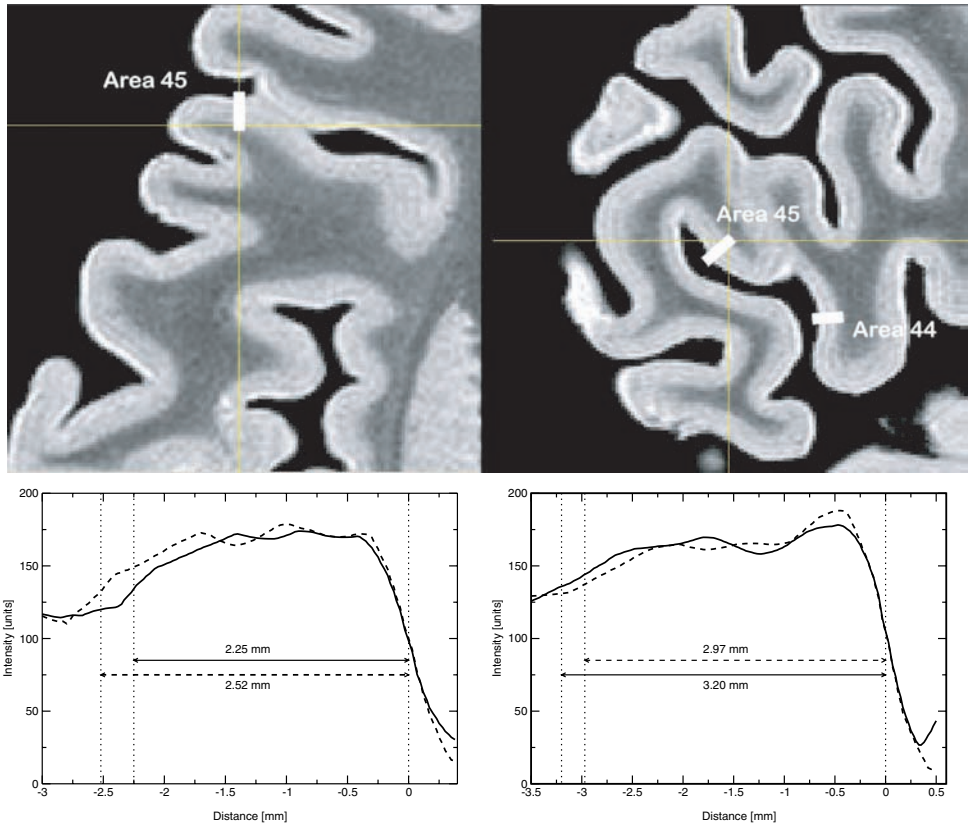

Fig. 15. Top: Axial (enlarged) and sagittal section through the inferior frontal gyrus. The profile denoted Area 45 was taken from the *pars triangularis*, while the other profile (Area 44) corresponds to the *pars opercularis*. Below: Intensity profiles through Area 45 (left) and Area 44 (right). The cortex is thinner in Area 45, but exhibits a more prominent banded structure.

line profiles also indicate that the MR intensity line profile is most similar to the low-magnification myelin stain intensity line profile."

It is unclear how the well-known cortical cellular and fiber structure translates into intensity profiles as revealed by high-resolution MRI in fixated brains. There is a striking similarity of MRI intensity profiles with photometric studies of the myeloarchitecture.[13,14] In addition, theoretical studies[12] demonstrated the equivalence of Nissl-stained cytometric intensity profiles with myelin-stained profiles. A quantitative comparison of MRI intensity profiles with optical profiles of stained tissue is necessary.

- "Using image processing techniques it is possible to detect regional characteritics of the fine-structure that allow segmentation into neocortical fields."

  Results shown for three different brain areas demonstrate the feasibility of analyzing the neocortical substructure from high-resolution MRI data. Using statistical

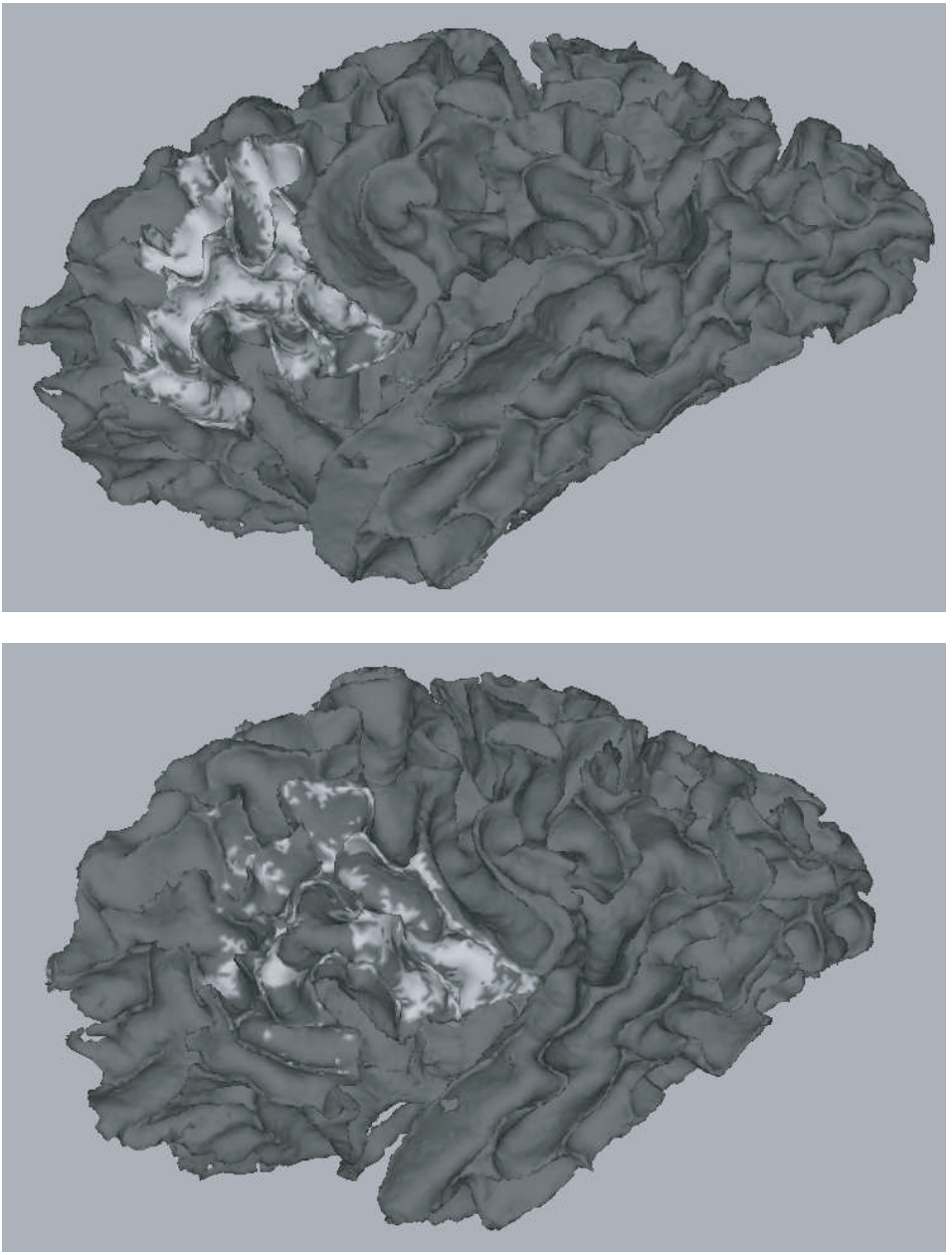

Fig. 16. Lateral view of the white matter surface. Area 45 (top) and Area 44 (below) were detected from model positions shown in Fig. 15 at a detection threshold of $z_{sim} \geq 2$ (Area 45) resp. $z_{sim} \geq -1$ (Area 44).

descriptors of the profiles obtained from a template region, the extent of target regions was determined by comparing local descriptors with the template. Qualitative properties of MRI intensity profiles and quantitative descriptors (e.g. cortical thickness, band position and width) corresponded well with descriptions found in reference publications based on histological examinations.

It is an open issue how much the approach described here may be translated to *in vivo* studies. Our scanning time of 12 h is impossible to sustain for humans, and might even be hard to achieve when scanning anaethesized animals (e.g. monkeys). Nevertheless, progress in MR techniques (especially at ultra-high field strengths and/or using array receiver coils) will offer a significant reduction in scanning times, and let us expect to have such scanning techniques at our disposal within this decade. The resolution obtained in current *in vivo* studies[4,36] is considered as too low to allow a reliable segmentation. Of course, with increasing resolution, unavoidable motion artefacts (e.g. from random head movements, swallowing, breathing and pulsation) influence the scan quality. Gated measurements may offer a solution.

The possibility of studying the neocortical fine-structure by MR imaging, i.e. introducing a myeloarchitecture-related parcellation of an individual brain, offers exciting perspectives for the analysis of structure-function relationships in the brain on a mesoscopic level.

Acknowledgments

The author would like to thank Prof. Th. Arendt and M. K. Brückner (Paul-Flechsig-Institut für Hirnforschung, Leipzig) for providing the specimen, C. J. Wiggins (MPI für Kognitions- und Neurowissenschaften, Leipzig) for MRI acquisition, and F. Föhlisch for performing the registration of histological slices with the MR images. This work was supported by a grant from the Interdisziplinäres Zentrum für Klinische Forschung (IZKF), University of Leipzig, under project C15.

References

1. K. Amunts, V. Istomin, A. Schleicher and K. Zilles, *Anat. Embryol.* **192** (1995) 557.
2. K. Amunts, F. Schmidt-Passos, A. Schleicher and K. Zilles, *Anat. Embryol.* **196** (1997) 393.
3. K. Amunts, A. Schleicher, U. Bürgel, H. Mohlberg, H. B. M. Uylings and K. Zilles, *J. Comp. Neurol.* **412** (1999) 319.
4. E. L. Barbier, S. Marrett, A. Danek, A. Vortmeyer, P. van Gelderen, J. Duyn, P. Bandettini, J. Grafman and A. P. Koretsky, *Magn. Reson. Med.* **48** (2002) 735.
5. K. Brodmann, *Die vergleichende Lokalisationslehre der Großhirnrinde* (Barth, Leipzig, 1909).
6. P. Cignoni, F. Ganovelli, C. Montani and R. Scopigno, *Comp. Graph.* **24**, 399.
7. A. M. Dale and M. I. Sereno, *J. Cogn. Neurosci.* **5** (1993) 162.
8. D. Eberly, http://www.magic-software.com/graphics/src/dist/pt3tri3.pdf, 1999.

9. G. M. Fatterpekar, T. P. Naidich, B. N. Delman, J. G. Aguinaldo, S. H. Gultekin, C. C. Sherwood, P. R. Hof, B. P. Drayer and Z. A. Fayad, *Am. J. Neuroradiol.* **23** (2002) 1313.
10. M. Garland and P. S. Heckbert, *J. Comp. Geom.* **14** (1999) 49.
11. S. Geyer, A. Schleicher and K. Zilles, *Neuroimage* **10** (1999) 63.
12. B. Hellwig, *J. Hirnforsch.* **34** (1993) 387.
13. A. Hopf, *J. Hirnforsch.* **10** (1968) 259.
14. A. Hopf, *J. Hirnforsch.* **10** (1968) 285.
15. F. Kruggel and G. Lohmann, in *Computer Aided Radiology (CAR'96)*, eds. H. U. Lemke, K. Inamura, C. C. Jaffe, M. W. Vannier (Elsevier, Amsterdam, 1996), p. 323.
16. F. Kruggel, D. Y. von Cramon, in *Workshop on Mathematical Models in Biomedical Image Analysis*, ed. B. Kimia (IEEE Press, Los Alamitos, 2000), p. 154.
17. F. Kruggel, M. K. Brückner, Th. Arendt, C. J. Wiggins and D. Y. von Cramon, in *Information Processing in Medical Imaging*, eds. M. F. Insana and R. M. Leahy (Springer, Heidelberg, 2001), LNCS 2982, p. 239.
18. F. Kruggel, M. K. Brückner, Th. Arendt, C. J. Wiggins and D. Y. von Cramon, *Med. Imag. Anal.* **7**, p. 251.
19. J. H. Lee, M. Garwood, R. Menon, G. Adriany, P. Andersen, C. L. Truwit and K. Ugurbil, *Magn. Reson. Med.* **34** (1995) 308.
20. G. Lohmann and D. Y. von Cramon, in *Workshop on Biomedical Image Analysis (Santa Barbara)*, (IEEE Computer Press, Los Alamitos, 1998), p. 24.
21. W. E. Lorensen and H. E. Cline, in *Computer Graphics (SIGGRAPH '87 Proceedings)*, (IEEE Computer Press, Los Alamitos, 1987), p. 163.
22. D. MacDonald, N. Kabani, D. Avis and A. C. Evans, *Neuroimage* **12** (2000) 340.
23. D. L. Pham and J. L. Prince, in *Information Processing in Medical Imaging*, eds. J. Duncan and G. Gindi, LNCS **1613** (Springer, Heidelberg, 1999), p. 140.
24. J. Rademacher, V. S. Caviness, H. Steinmetz and A. M. Galaburda, *Cereb. Cortex* **3** (1993) 313.
25. G. Rajkowska and P. S. Goldman-Rakic, *Cereb. Cortex* **5** (1995) 307.
26. G. Rajkowska and P. S. Goldman-Rakic, *Cereb. Cortex* **5** (1995) 323.
27. S. A. Sakissov, I. N. Filimonov, E. P. Kononowa, I. S. Preobraschenskaja and L. A. Kukuew, *Atlas of the Cytoarchitectonics of the Human Cerebral Cortex* (Medgiz, Moscow, 1995).
28. A. Schleicher and K. Zilles, *J. Microscopy* **157** (1990) 367.
29. A. Schleicher, K. Amunts, S. Geyer, P. Morosan and K. Zilles, *NeuroImage* **9** (1998) 165.
30. D. W. Shattuck and R. Leahy, *IEEE Trans. Med. Imag.* **20** (2001) 1167.
31. D. Terzopoulos and K. Fleischer, *Vis. Comp.* **4** (1988) 306.
32. P. Thevenaz, T. Blu and M. Unser, in *Handbook of Medical Image Processing* (Academic Press, San Diego, 2000), p. 393.
33. J. Toriwaki and T. Yonekura, *Forma* **17** (2002) 183.
34. C. Vogt and O. Vogt, *J. Psych. Neurol.* **25** (1919) 279.
35. C. von Economo, *Zellaufbau der Großhirnrinde des Menschen* (Springer, Wien, 1927).
36. N. B. Walters, G. F. Egan, J. J. Kril, M. Kean, P. Waley, M. Jenkinson and J. D. G. Watson, *Proc. Natl. Acad. Sci.* **100** (2003) 2981.
37. C. Xu and J. L. Prince, *IEEE Trans. Imag. Proc.* **1998** (1998) 359.
38. K. Zilles, R. Werners, U. Büsching and A. Schleicher, *Anat. Embryol.* **174** (1986) 339.